The Journal of Experimental Biology 207, 1825-1841
Published by The Company of Biologists 2004
doi:10.1242/jeb.00968

The hydrodynamics of eel swimming

I. Wake structure

Eric D. Tytell* and George V. Lauder

Department of Organismic and Evolutionary Biology, Harvard University, Cambridge, MA 02138, USA

*Author for correspondence (e-mail: tytell@oeb.harvard.edu)

Accepted 8 March 2004

Summary

Eels undulate a larger portion of their bodies while swimming than many other fishes, but the hydrodynamic consequences of this swimming mode are poorly understood. In this study, we examine in detail the hydrodynamics of American eels (*Anguilla rostrata*) swimming steadily at 1.4 L s^{-1} and compare them with previous results from other fishes. We performed high-resolution particle image velocimetry (PIV) to quantify the wake structure, measure the swimming efficiency, and force and power output. The wake consists of jets of fluid that point almost directly laterally, separated by an unstable shear layer that rolls up into two or more vortices over time. Previously, the wake of swimming eels was hypothesized to consist of unlinked vortex rings, resulting from a phase offset between vorticity distributed along the body and vorticity shed at the tail. Our high-resolution flow data suggest that the body anterior to the tail tip produces relatively low vorticity, and instead the wake structure results from the instability of the shear layers separating the lateral jets, reflecting pulses of high vorticity shed at the tail tip. We compare the wake structure to large-amplitude elongated body theory and to a previous computational fluid dynamic model and note several discrepancies between the models and the measured values. The wake of steadily swimming eels differs substantially in structure from the wake of previously studied carangiform fishes in that it lacks any significant downstream flow, previously interpreted as signifying thrust. We infer that the lack of downstream flow results from a spatial and temporal balance of momentum removal (drag) and thrust generated along the body, due to the relatively uniform shape of eels. Carangiform swimmers typically have a narrow caudal peduncle, which probably allows them to separate thrust from drag both spatially and temporally. Eels seem to lack this separation, which may explain why they produce a wake with little downstream momentum while carangiform swimmers produce a wake with a clear thrust signature.

Key words: eel, *Anguilla rostrata*, wake structure, particle image velocimetry, fish, swimming, fluid dynamics, efficiency.

Introduction

Different fishes swim in different ways. To categorize this diversity, fish swimming is usually classified into a variety of different modes. A primary grouping distinguishes several modes among fishes that use their body and caudal fin primarily for propulsion. In particular, eel-like, or ‘anguilliform’, fishes undulate a large portion of their bodies, while jack-like, or ‘carangiform’, fishes undulate much less (Breder, 1926; Webb, 1975). These kinematic distinctions have been recognized for many years, even before Breder gave them their modern names in 1926 (Alexander, 1983), but the hydrodynamic consequences of the differences in kinematics are not well understood.

Most modern studies on the hydrodynamics of fish swimming have been done on carangiform swimmers. These fishes tend to have fusiform or laterally compressed bodies, often with a pronounced caudal peduncle. The greatest lateral excursions occur near the peduncle and the caudal fin (Webb, 1975), although there may be some yawing motions at the head (Donley and Dickson, 2000). In addition, researchers have distinguished several gradations of carangiform swimming, from subcarangiform, in which a greater proportion of the body undulates, to thunniform, in which the tail moves largely independently of the body (Webb, 1975). While swimming, carangiform fishes produce a series of vertical linked vortex rings, angled to the swimming direction (Müller et al., 1997; Triantafyllou et al., 2000; Drucker and Lauder, 2001; Nauen and Lauder, 2002a).

The hydrodynamics of anguilliform swimming have been studied much less. Like the eel, after which this mode is named, anguilliform swimmers tend to be elongate with little or no narrowing at the caudal peduncle. This lack of separation between the body and tail is particularly extreme in eels, in which the dorsal, caudal and anal fins effectively form a continuous median fin (Helfman et al., 1997). In other

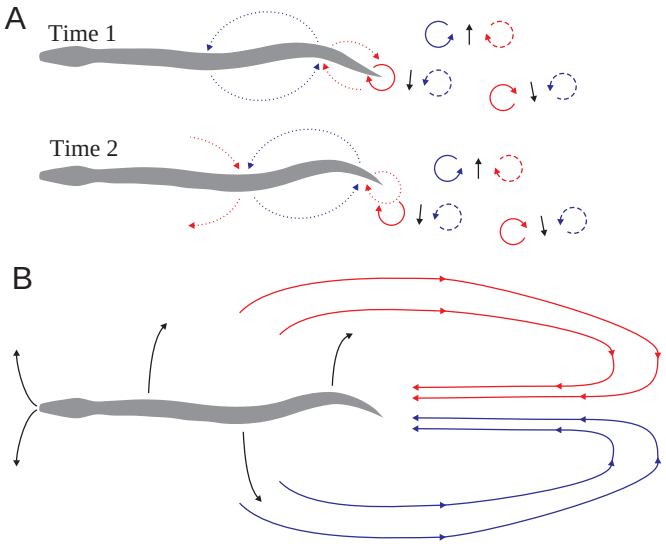

Fig. 1. Flow fields behind swimming eels according to two previous studies. Red arrows indicate flow with clockwise rotation and blue arrows indicate counter-clockwise rotation. (A) Results from Müller et al. (2001), showing the wake structure they observed. Proto-vortices (dotted lines) appear to be vortices centered on the body that progress down the body. After they are shed into the wake they are shown as dashed lines. They are shed after the stop/start vortex (solid lines), resulting in two same-sign vortices being shed each tail beat. (B) Computational fluid dynamic model of Carling et al. (1998). The model indicates a large flow wrapping around the eel, resulting in a net upstream flow in the wake behind the eel.

anguilliform swimmers, such as sharks and needlefish, the fins are more separated and there may be a slight narrowing at the caudal peduncle (Liao, 2002). They undulate from one-third to almost all of their bodies, depending on speed, often with one or more complete waves present at a time (Gillis, 1998). These extra undulations, relative to carangiform swimmers, must affect the flow around their bodies and in the wake, but the effect is not well understood.

Lighthill's elongated body theory (referred to here as EBT) offers some insight into the possible effect of different kinematics (Lighthill, 1971). He argues that the carangiform mode is more efficient, because his theory predicts that thrust is produced only at the trailing edge of the tail. Therefore, any extra body undulation is wasted energy, and efficient swimmers should undulate as little of their body as possible. Indeed, many pelagic predators considered highly efficient (Lighthill, 1970; Barrett et al., 1999) are thunniform swimmers and hold their bodies relatively straight. EBT, however, is a simple model, and neglects many effects, including viscous forces, which could enable thrust production along the length of an anguilliform fish's body (Taneda and Tomonari, 1974; Shen et al., 2003).

Only two recent studies (Carling et al., 1998; Müller et al., 2001) address the hydrodynamics of eel-like swimming, and they offer divergent conclusions. Müller et al. (2001) used particle image velocimetry (PIV; Willert and Gharib, 1991) to observe the flow fields around freely swimming juvenile eels. Based on their observations, they hypothesized that eels' wakes consist of unlinked vortex rings moving laterally (Fig. 1A). They proposed that eels shed two separate same-sign vortices because of a lag between the stop/start vortex (solid arrows in Fig. 1A), shed when the tail changes direction, and centers of rotation that progress down the body, which they termed 'proto-vortices' (broken arrows in Fig. 1A). They did not observe a downstream jet behind the tail, which is typical of carangiform wakes (e.g. Nauen and Lauder, 2002a). Due to the difficulty of working with freely swimming eels, Müller and colleagues did not evaluate the effects of different swimming speeds on the wake structure. Also, the mechanical significance of the difference between carangiform wakes and the wake they observed for eels remains unclear.

By contrast, Carling et al. (1998) used a two-dimensional computational fluid dynamic model to estimate the flow fields behind a self-propelled 'eel-like' anguilliform swimmer. Their calculations indicated a single, large vortex ring wrapping around the eel, with the eel in the center, producing upstream flow behind the eel (Fig. 1B). These results suggest that eels produce thrust almost exclusively along the body, but not at the tail tip, which seems to result mostly in drag. Carling's model, while tested thoroughly in several standard test cases (Carling, 2002), has not been verified on living eels.

Several important questions remain. Which of these two views of anguilliform wake flow patterns are correct? What are the quantitative differences between anguilliform and carangiform wakes? How do these differences affect the swimming performance? How efficient hydrodynamically is anguilliform swimming relative to carangiform swimming? In particular, Lighthill's (1970) argument for the inefficiency of anguilliform swimming leads to an inconsistency: eels migrate thousands of kilometers without feeding (van Ginneken and van den Thillart, 2000), and many anguilliform sharks swim constantly (Donley and Shadwick, 2003). It is unlikely that such proficient swimmers are highly inefficient. In fact, a recent study of swimming energetics found that the physiological cost of migration for eels was low (van Ginneken and van den Thillart, 2000).

In the present study, therefore, we examine in detail the wake of the American eel, *Anguilla rostrata*, swimming steadily at a single speed. The flow around anguilliform swimmers is compared with both previous models and with previous data from carangiform swimmers. We propose a new explanation of the hydrodynamic differences between anguilliform and carangiform swimming, emphasizing the importance of carangiform swimmers' narrow caudal peduncle and propeller-like caudal fin over the importance of differences in kinematics. In addition, we provide the first quantitative comparison of the predictions of EBT (Lighthill, 1971) to empirical forces estimated using PIV and demonstrate a partial correlation. Finally, we examine the efficiency and power output for steadily swimming eels.

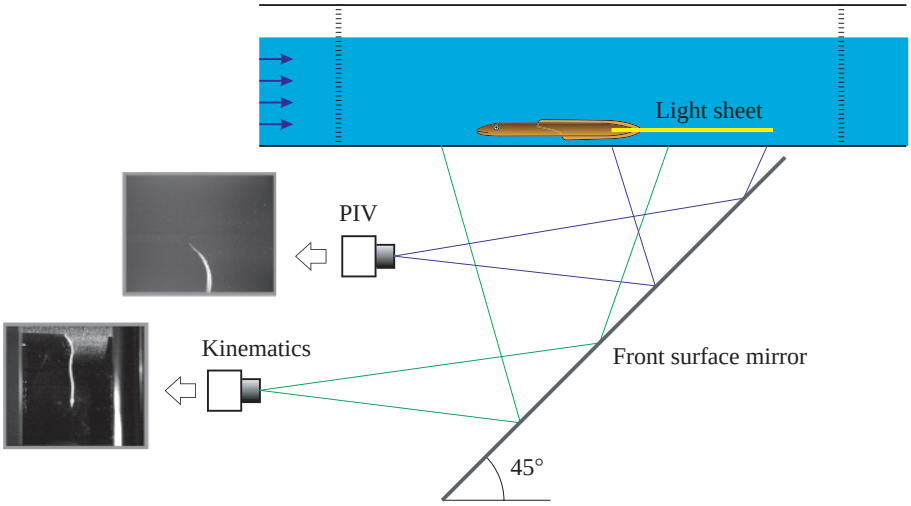

Fig. 2. Methods. Eels were filmed from below using two synchronized high-speed cameras aimed at a 45° mirror below the flow tank. A laser light sheet 7 mm above the bottom of the tank illuminated the eel's wake and part of its tail. One camera (labeled 'kinematics') imaged the whole eel, and the other camera (labeled 'PIV') imaged the light sheet. Representative images from each camera are shown to the left. Diagram is not to scale.

Materials and methods

Animals and experimental procedure

We obtained American eels, *Anguilla rostrata* LeSueur, by seine from the Charles River, Cambridge, MA, USA during June and July 2002 and housed them in aquaria at room temperature with a 12 h:12 h light:dark cycle. We performed experiments on 11 individuals, ranging from 8 cm to 23 cm total body length (L), in a 600-liter recirculating flow tank with a 26 cm×26 cm×80 cm working section. Three individuals (L=20 cm, 20 cm and 23 cm, corresponding to masses of 14 g, 16 g and 14 g) that swam exceptionally steadily were chosen for detailed analysis. Before the experiment, an eel was moved from its tank to the flow tank and allowed to acclimate. Animals were confined to the working section using plastic grids upstream and downstream with 5 cm×5 cm holes covered in a fine mesh. After an acclimation period of approximately 1 h in flow of ~1 L s^{-1}, the eels spontaneously adopted steady swimming behavior on the bottom of the flow tank. The eels would not swim consistently in a mid-water plane and, since eels often naturally swim on the bottom in rivers during daylight (Smith and Tighe, 2002), we focused on eels swimming in that region. This also allowed comparison with previous work by Gillis (1998) that studied eels swimming on the bottom.

All data were taken from eels swimming at ~1.4 L s^{-1}, ranging from 1.30 to 1.44 L s^{-1}. In total, the swimming kinematics for 415 tail beats were analyzed. The hydrodynamics of 118 of these were examined. Considerable effort was expended to analyze only truly steady swimming sequences; all sequences analyzed had a maximum variation in velocity under ±5%; in most cases, the velocity varied by less than ±3%; and the S.D. in velocity over all sets was 2%. In addition, most sequences involved 10 or more sequential steady tail beats. During the experiments, an eel was gently maneuvered into position using a wooden probe. Care was taken to remove the probe completely from the region around the eel before data were taken.

The eels were filmed from below through a mirror inclined at 45° with two high-speed cameras, one to record the swimming kinematics and one to film the light sheet for PIV (Fig. 2). An approximately 30 cm-wide horizontal light sheet was projected 7 mm above the bottom of the tank, along the dorso-ventral midline of the eels, using two argon-ion lasers operating at ~4 W and 8 W, respectively. The light from the two lasers was combined optically to form a single large light sheet. The eels' swimming kinematics were recorded using a RedLake digital camera at 250 or 125 frames s^{-1}. For PIV, a close-up view of the light sheet was filmed using either a RedLake digital camera at 250 frames s^{-1} at 480 pixel×420 pixel resolution or a NAC Hi-DCam at 500 frames s^{-1} at 1280 pixel×1024 pixel resolution. A six-point calibration between the two cameras allowed positions to be converted between the two images with an error of ~0.5 mm using a linear rotation and scaling transformation (Matlab 6.1 imtransform routine; Mathworks, Inc., Natick, MA, USA)

Kinematics

Eel outlines and midlines were digitized automatically using a custom Matlab 6.1 (Mathworks, Inc.) program. The positions of the head and tail were identified manually. The eel midline was then located by performing a 1-D cross-correlation analysis along transects between the head and the tail, to find the bright region with a width corresponding to the known width of the eel. This technique produced fewer errors resulting from the presence of PIV particles in portions of the images than thresholding-based techniques used in previous kinematic studies (e.g. Tytell and Lauder, 2002). A similar method located the edges of the eel's image. Twenty points were identified along the midline and were simultaneously smoothed temporally and spatially using a 2-D tensor product spline (Matlab's spaps routine), a two-dimensional analog of an optimal method ('MSE' method in Walker, 1998). The tensor product spline, however, does not allow a direct specification of the mean error on the data as in the 1-D version. Thus, the smoothing values were initially set at 0.5 pixel, the limit of measurement accuracy from the video, and adjusted manually until a good fit was reached. This resulted in a mean distance between the smoothed and measured values of less than 0.3 pixel (approximately 0.2 mm).

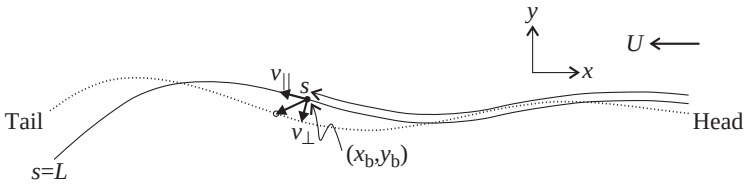

Fig. 3. Coordinate system used for elongated body theory calculations. The solid line represents a midline at one time, while the dotted line represents it at a later time. Perpendicular and parallel velocity, $v_\perp$ and $v_{||}$, are shown as vectors at the point (x_b, y_b). The arc length s is shown along the midline and the eel is swimming into a flow U. L is total body length.

Kinematic variables, including amplitude at each body point, tail beat frequency, body wave length and body wave velocity, were calculated by finding the peaks in the lateral excursion of each point over time. A Matlab program automatically located the peaks based on the midlines, as estimated above. The amplitude, frequency and wave length were determined by the timing, position and height of the peaks. Average side-to-side tail velocity was estimated as $4A/f$, where A is amplitude and f is frequency. The body wave velocity was determined by the slope of the line fitted to the wave peak position (in distance down the body) and the time of that wave peak.

The forces and power required for swimming were calculated using large-amplitude EBT (Lighthill, 1971). The time-varying thrust (F_{thrust}) and lateral force ($F_{lateral}$) are:

$$F_{thrust} = \left[mv_\perp \frac{\partial y_b}{\partial t} + \tfrac{1}{2} m v_\perp^2 \frac{\partial x_b}{\partial s} \right]_{s=L} + \frac{\partial}{\partial t} \int_0^L m v_\perp \frac{\partial y_b}{\partial s}\, ds$$

$$F_{lateral} = \left[-mv_\perp \left(\frac{\partial x_b}{\partial t} + U \right) + \tfrac{1}{2} m v_\perp^2 \frac{\partial y_b}{\partial s} \right]_{s=L} - \frac{\partial}{\partial t} \int_0^L m v_\perp \frac{\partial x_b}{\partial s}\, ds , \quad (1)$$

where $x_b(s,t)$ and $y_b(s,t)$ are the position of points along the midline of an eel facing in the positive x direction in flow with velocity U towards the eel, m is the virtual mass per unit length, L is the eel's length, s is the distance along the midline from head to tail, t is time and $v_\perp$ is the body velocity perpendicular to the midline:

$$v_\perp = \frac{\partial x_b}{\partial t}\frac{\partial y_b}{\partial s} - \frac{\partial y_b}{\partial t}\frac{\partial x_b}{\partial s} + U \frac{\partial y_b}{\partial s} . \quad (2)$$

Fig. 3 shows the coordinate system and variable definitions. The wasted power (P_{wake}) shed into the wake is $\frac{1}{2}[m v_\perp^2 v_{||}]_{s=L}$, where $v_{||}$ is the velocity parallel to the midline:

$$v_{||} = \frac{\partial x_b}{\partial t}\frac{\partial x_b}{\partial s} - \frac{\partial y_b}{\partial t}\frac{\partial y_b}{\partial s} + U \frac{\partial x_b}{\partial s} . \quad (3)$$

Additionally, the position of the proto-vortices along the eel's body was estimated according to Müller et al. (2001) by searching for the points along the body where lift (F_{lift}) equals zero, defined using small-amplitude EBT (Lighthill, 1960) as:

$$F_{lift} = \tfrac{\pi}{4} \rho h^2 (\partial/\partial t + U\partial/\partial s)(\partial y_b/\partial t + U \partial y_b/\partial s) , \quad (4)$$

where ρ is the water density and h is the dorso-ventral height of the eel. Because of the error introduced by taking second derivatives of values with measurement error, an analytical expression for the midline position was used to find the zero lift positions. Using the kinematic values measured, y_b can be expressed as $Ae^{\alpha(s-1)} \sin k(s-Vt)$, where A is the tail beat amplitude, α is a parameter defining how fast the amplitude grows from head to tail, k is the wave number (equal to 2π/wave length), and V is the body wave speed.

Hydrodynamics

High-resolution PIV was performed using a custom Matlab 6.1 program in two passes using a standard statistical cross-correlation (Fincham and Spedding, 1997) and a Hart (2000) error correction technique with an integer pixel estimate of the velocity between passes (as in Westerweel et al., 1997; Hart, 1999). PIV interrogation regions were about 5 mm×5 mm and 2.5 mm×2.5 mm in coarse and fine pass, respectively, with search regions of 9 mm×9 mm and 3.5 mm×3.5 mm. For the lower resolution video, this produced a matrix 68×78 vectors, and for the higher resolution, 100×125 vectors. Data were smoothed and interpolated onto a regular grid using an adaptive Gaussian window algorithm with the optimal window size (2–3 mm for these data; Agüí and Jiménez, 1987; Spedding and Rignot, 1993), being careful to note the inherently uneven spacing of PIV data (Spedding and Rignot, 1993). The Gaussian window method was used because it provides good results (Fincham and Spedding, 1997) while being simple and fast when applied to such large matrices of vectors.

Boundary layers and background flow

Because eels swam on the bottom of the flow tank, we made a series of measurements to quantify the flow regime in this part of the flow tank and to be certain that we were observing free-stream flow. At all swimming speeds, the PIV light sheet was above the flow tank boundary layer, which was turbulent. The boundary layer was quantified using a vertical light sheet, showing that the boundary layer thickness (δ) was equal to ~7 mm at the slowest flow speed used (Fig. 4). The boundary layer changes from laminar to turbulent just below that speed, indicating that the boundary layers in all data sets were turbulent. At speeds above this transition, the boundary layer is always thinner, decreasing proportionally to the free-stream velocity to the –1/5 power (Schlichting, 1979). Thus, at the highest speed used, ~40 cm s^{-1}, we estimated the boundary layer to be ~5.5 mm thick.

Because the boundary layer was turbulent, the background flow was complex. Turbulent boundary layers are characterized by a range of relatively long-lived, coherent structures that rise up out of the boundary layer region

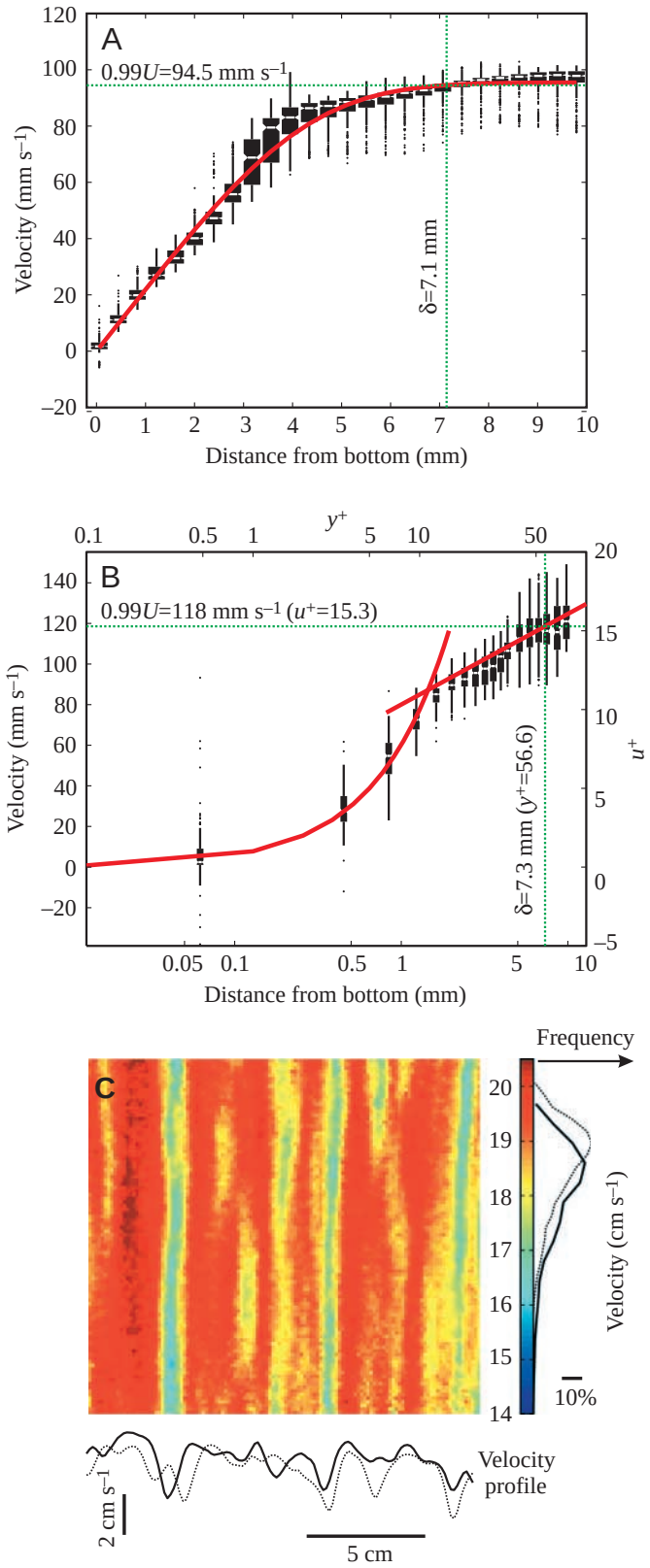

Fig. 4. Flow tank boundary layer. The boundary layer thickness was 7.3 mm or less at all swimming velocities. Black boxes are standard statistical box plots, with the box stretching from the 25th to 75th quartile, a white line at the median, and whiskers of 1.5 times the interquartile range. Outliers are shown as separate points. (A) Laminar boundary layer at flow speeds less than 95 mm s^{-1} with fit Blasius boundary layer profile (Faber, 1995). The boundary layer thickness at 0.99U was 7.3 mm (green dotted lines). (B) Turbulent boundary layer at flow speeds above 120 mm s^{-1}. The normalized distance y^+ and velocity u^+ are shown on the top and right, respectively. The law of the wall profile for turbulent boundary layers, $u^+=5.75 \log y^+ + 5.2$, is shown in red. Note that this is a semi-log plot. (C) Axial component of velocity from the horizontal light sheet, 7 mm above the bottom, showing turbulent effects. Flow is from bottom to top. Note the streamwise regions of reduced velocity. The bottom profile shows mean velocity (solid line) and mean velocity about two hours later (dotted line). A histogram of velocities (solid line) is also shown beside the color bar with a histogram from about two hours later (dotted line).

(Robinson, 1991). In particular, structures called 'quasi-streamwise vortices' were common. In our data, quasi-streamwise vortices, which are vortex lines oriented approximately parallel to the flow (Robinson, 1991), were visible as streamwise regions of slower or angled flow (Fig. 4C). Conveniently, they were consistent over a duration of many minutes.

The consistency of the turbulent structures enabled us to subtract their effect from the flow. For each swimming speed, we took 50 flow fields without the eel present. These fields were then averaged to estimate a mean background flow, which was subtracted from the wake data to remove the turbulent effects. The background velocity changed spatially by as much as 13% cm^{-1} but changed over time by only about 0.1% s^{-1} (Fig. 4C).

Wake analysis

Wakes were only analyzed when the kinematics remained steady for at least three tail beats. Most wakes analyzed included between five and 15 consecutive steady tail beats. Phase-averaged wake vector fields were produced by averaging frames corresponding to the same tail-beat phase, dividing the tail beat into 20 steps. These phase-averaged fields are instructive for visualization, but no quantitative values were measured from them.

Vortex centers were digitized manually. Location of the vortices in the vector fields was aided by plotting the discriminant for complex eigenvalues (DCEV; Vollmers, 1993; Stamhuis and Videler, 1995):

$$(\partial u/\partial x + \partial v/\partial y)^2 - 4(\partial u/\partial x\, \partial v/\partial y - \partial u/\partial y\, \partial v/\partial x)\,, \qquad (5)$$

where u and v are the x and y components of velocity, respectively. DCEV is negative in regions where the fluid is rotating more than it is diverging. Two vortices were identified for each half tail beat. When the tail changes direction, it sheds a primary vortex. As the tail moves to the other side, it stretches the primary vortex into a shear layer, which eventually rolls up, producing a secondary vortex. The vortex circulation was determined by integrating a circle at an 8 mm radius from the vortex core. This radius was determined by inspecting the

circulation values at increasing radii for many vortices. Finally, the width of the lateral jet was determined by the pair of vortices on either side (the primary vortex of one half tail beat and the secondary vortex of the next). These are the two vortices identified by Müller et al. (2001) as the cores of a vortex ring. The angle of the line between the two vortices and the mean jet velocity in the region between them were determined. Finally, the velocity along the center line between the two vortices was integrated to get another measure of circulation.

Assuming that the two vortices on either side of the lateral jet are the cores of a small-core vortex ring, the impulse (I) of the ring was estimated as (Faber, 1995):

$$I = \tfrac{1}{4}\pi\rho\Gamma h d\,, \quad (6)$$

where Γ is circulation across the center line of the vortex ring, h is the height of the ring, equivalent to the eel's height, and d is the diameter in the plane of the light sheet. The rings are assumed to be elongated ovals, with the height equal to the height of the eels, 10 mm, as previously observed in other fishes (Lauder, 2000; Drucker and Lauder, 2001; Nauen and Lauder, 2002a). The mean force (F_{PIV}) that produced the vortex ring was also estimated by dividing the impulse by half the tail beat period.

The power (P) that the eel added to the fluid was determined by integrating across a plane approximately 8 mm behind the tail tip:

$$P = \tfrac{1}{2}\rho U h \int_{-w}^{w} [(u+U)^2 + v^2] - U^2\, dy = \tfrac{1}{2}\rho U h \int_{-w}^{w} u^2 + 2Uu + v^2\, dy\,, \quad (7)$$

where h is the height of the area affected by the eel, equivalent to the eel's height, and w is the half-width of the wake (~40 mm). Because of the uncertainty introduced by the quasi-streamwise vortices, and because almost all of the wake velocity was lateral, a 'lateral' power (P_{lateral}) was calculated using only the v component of velocity:

$$P_{\mathrm{lateral}} = \tfrac{1}{2}\rho U h \int_{-w}^{w} v^2\, dy\,. \quad (8)$$

To account for the phase lag between when the kinetic energy was shed at the tail and when it reached the position x_{plane} where power was measured in the wake, the phasing of the wake power was adjusted by $2\pi x_{\mathrm{plane}} f/U$.

Force, impulse and power were both normalized to produce force and power coefficients. Using coefficients is important because it makes these values comparable between eels of different sizes and between the present and other studies (Schultz and Webb, 2002). The normalization factors for force and power were the standard $\frac{1}{2}\rho S U^2$ and $\frac{1}{2}\rho S U^3$, respectively, where S is the wetted surface area of the eel (Faber, 1995). No standard normalization exists for impulse, however. Since impulse is in units of force × time, we chose to normalize by the standard characteristic force $\frac{1}{2}\rho S U^2$ and a characteristic time L/U, resulting in an impulse normalization factor of $\frac{1}{2}\rho S L U$.

Statistics

The kinematics in the data set used for PIV measurements were compared with those in the complete data set to make sure that the swimming behavior in the selected data was typical. A mixed-model multivariate analysis of variance (MANOVA; Zar, 1999) was performed on the kinematic variables, including the individual as a random effect and which set the data came from (i.e. the PIV or complete data sets) as a fixed effect. The kinematic differences between individuals in the PIV data set were also assessed using a MANOVA including only the effect of individual variation.

The changes in wake morphology over time were examined by regressing individual wake morphology parameters on tail-beat phase, including the individual as a random effect. Significant slopes were determined by testing the significance of variation in time over the variation due to the interaction by individuals with time, as in a mixed-model analysis of variance (ANOVA).

A repeated-measures ANOVA (Zar, 1999) was performed to compare the initial circulation of the primary vortex to the sum of the circulations of the primary and secondary vortices, after they divided. Circulation at two different times was the repeated measure, which allowed the early primary vortex circulation to be compared with the sum of the primary and secondary vortex circulations later in time. The individual was included as a random factor (Zar, 1999).

Finally, mixed-model ANOVAs were used to compare force, power and impulse estimates based on EBT (Lighthill, 1971) with those values measured using PIV. The individual was again included as a random factor.

All analyses were performed using Systat 10.2 (Systat Software, Inc., Point Richmond, CA, USA). All error values that are reported are standard error and include the number of data points, where appropriate.

Results

Kinematics

At the moderate swimming speed of ~1.4 $L\ s^{-1}$, all individuals swam very steadily and repeatably. For the three individuals studied in detail, swimming speed varied by a maximum of about ±4% and generally varied less than ±2%. At that speed, the animals swam with a tail-beat amplitude (A) of 7% of body length at a frequency (f) of 3.1 Hz. A and f are approximately inversely proportional to each other, even within this small speed range (r=–0.669). Thus, the product, the average tail velocity ($4Af$) over a period, and average Strouhal number are quite constant: 0.856±0.007 $L\ s^{-1}$ and 0.314±0.003, respectively. Body wave velocity was generally 1.878±0.006 $L\ s^{-1}$, resulting in slip of 0.73, an indication of the swimming efficiency (Lighthill, 1970). The body wave length

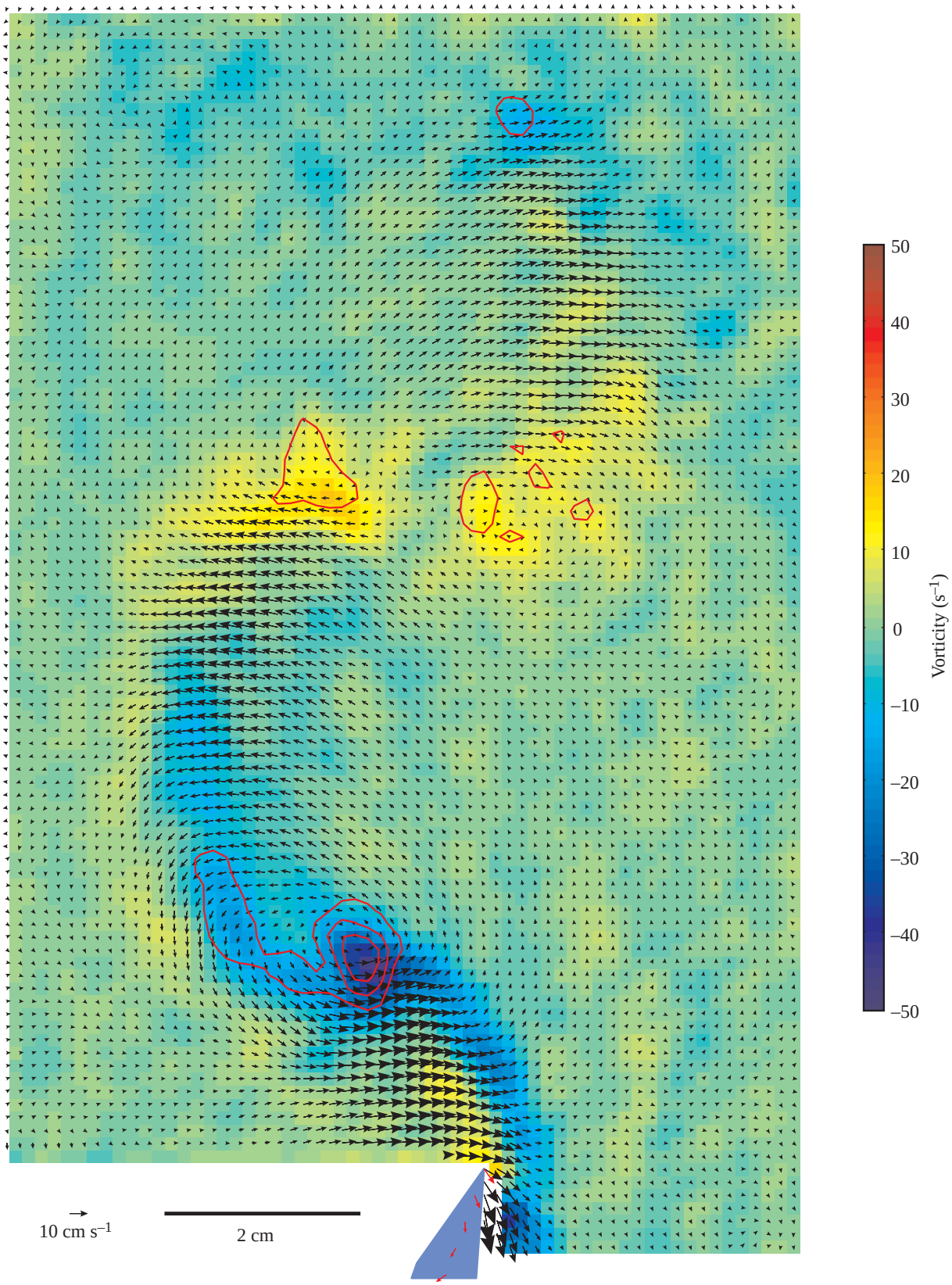

Fig. 5. Representative flow field from behind an eel at 90% of the tail beat cycle. The field is a phase average of 14 tail beats. Vorticity is shown in color in the background, and contours of the discriminant for complex eigenvalues at –200, –500 and –1000 are shown in red. The eel's tail is in blue at the bottom, with red arrows, scaled in the same way as the flow vectors, which indicate the motion of the tail. Vector heads are retained on vectors shorter than 2.5 cm s^{-1} to show the direction of the flow.

Table 1. *Kinematic parameters*

Variable	Symbol	Value ± S.E.M.	Units
Length	L	20.8±0.7*	cm
Swimming velocity	U	1.374±0.002	L s^{-1}
Reynolds number	Re	60 000	
Tail beat amplitude	A	0.0693±0.0005	L
Tail beat frequency	f	3.11±0.03	Hz
Body wave velocity	V	1.878±0.006	L s^{-1}
Body wave length		0.604±0.006	L
Average tail velocity	$4Af$	0.856±0.006	L s^{-1}
Strouhal number	St	0.314±0.003	
Slip	U/V	0.731±0.002	
Stride length	U/f	0.448±0.005	L
Amplitude growth parameter	α	2.759±0.009†	

N=118 except where indicated (*N=3; $^{\dagger}N$=2180).

Fig. 6. Velocity transects through vortices in the eel's wake over time. The center of the first vortex is shown by the vertical dotted lines, and zero velocity is indicated by the horizontal dotted lines. Representative flow fields are shown to the right, indicating the position of the transect, with vorticity shown in color. The cross identifies the position of the first vortex, and the circle identifies the position of the second. Standard error around each velocity trace is shown by a lighter-colored region. (A) Transects through the primary vortex and, once it is formed, the secondary vortex. Idealized profiles through a single Rankine vortex and two same-sign Rankine vortices are shown in black at top and bottom. The position of the secondary vortex, plus or minus standard error, is shown as a bar along the zero line. Before the secondary vortex is completely formed, this bar indicates the position of the inflection point in velocity where the vortex will be formed. (B) Transects across the lateral jet, from the secondary vortex of one half tail beat to the primary vortex of the next. An idealized profile through a small-core vortex ring is shown in black above.

was usually ~60% of body length, or ~1.65 waves on the body at any given time. Amplitude increased exponentially along the body as $Ae^{\alpha(s-1)}$, where s is the distance along the body, from 0 at the head to 1 at the tail, and α is a parameter that defines how fast the amplitude grows (r^2=0.978). α was equal to 2.76±0.01. A linear regression did not fit the data nearly as well; r^2 was 0.890 and the residuals were visibly non-normal. Kinematic parameters are summarized in Table 1.

To verify that the sequences chosen for hydrodynamic analysis were typical of overall swimming performance, we examined a larger data set containing 415 tail beats taken under the same conditions but in which the PIV data were not quantitatively analyzed. A MANOVA on four parameters (tail-beat amplitude and frequency, amplitude growth parameter, body wave length and slip) that completely define the kinematics did not show a significant difference between the larger data set and that used for hydrodynamic analysis (Wilk's lambda=0.978; $F_{4,409}$=1.858; P=0.101).

Swimming kinematics varied significantly among individuals. In most variables, individuals differed from one another by less than 10%. However, one individual consistently chose to swim with a higher amplitude (about 13% higher) and lower frequency (about 25% lower) than the others. Another individual used a longer body wave (about 20% longer) than the others. By contrast, wave velocity differed very little among individuals; all were within 5% of each other. While these differences were highly significant (MANOVA: Wilk's lambda=0.0139; $F_{10,200}$=149.5; P<0.001), most studies of this nature have significant variation among individuals (e.g. Shaffer and Lauder, 1985).

Given the average swimming kinematics, the predicted position of the proto-vortex was calculated analytically using equation 4. The proto-vortex is shed off the tail 16 ms after the tail reaches its maximum lateral excursion, or 5.1% of a tail-beat cycle later.

Hydrodynamics

In all 11 individuals, the wake consisted of lateral jets of fluid, alternating in direction, separated by one or more vortices or a shear layer (Fig. 5). Each time the tail changes direction, it sheds a stop/start vortex. As the tail moves to the other side, a low pressure region develops in the posterior quarter of the body, sucking a bolus of fluid laterally. The bolus is shed off the tail, stretching the stop/start vortex into an unstable shear layer, which eventually rolls up into two or more separate, same-sign vortices. The wake generally contains more total power than is predicted by large-amplitude EBT (Lighthill, 1971). These features are analyzed in detail below, focusing on the three individuals chosen for detailed quantitative study.

Wake morphology

The stop/start vortex, shed when the tail changes direction, is designated the 'primary' vortex. The vortex formed later, when the shear layer rolls up, is called the 'secondary' vortex. The primary vortex from one half tail beat and the secondary vortex from the next form the edges of each lateral jet. These two vortices appear to be the cores of a small-core vortex ring. However, without velocity data from the planes perpendicular to the one used in the present study, it is not certain that the vortices truly form a ring. To emphasize this difference, we will not call this region a vortex ring; instead, we term it the lateral jet.

To address how the wake changes over time, wake morphology parameters were regressed individually on tail-beat phase and individual, treating the individual as a random factor. In general, the wake widens over time and becomes weaker. The distance between the primary and secondary vortex increases at ~0.12 $L\,T^{-1}$, where T is a tail-beat period ($F_{1,2}$=28.7; P=0.033), during the approximately 1.5 T in which the wake was visible. The diameter of the lateral jet, however, stays approximately constant at 0.21 L throughout time ($F_{1,2}$=0.370; P=0.605). The two vortices on either side of the lateral jet (the 'vortex ring') stay parallel to the swimming direction ($F_{1,2}$=0.037; P=0.864), but the lateral jet itself is inclined slightly upstream, with an angle of 87° (significantly

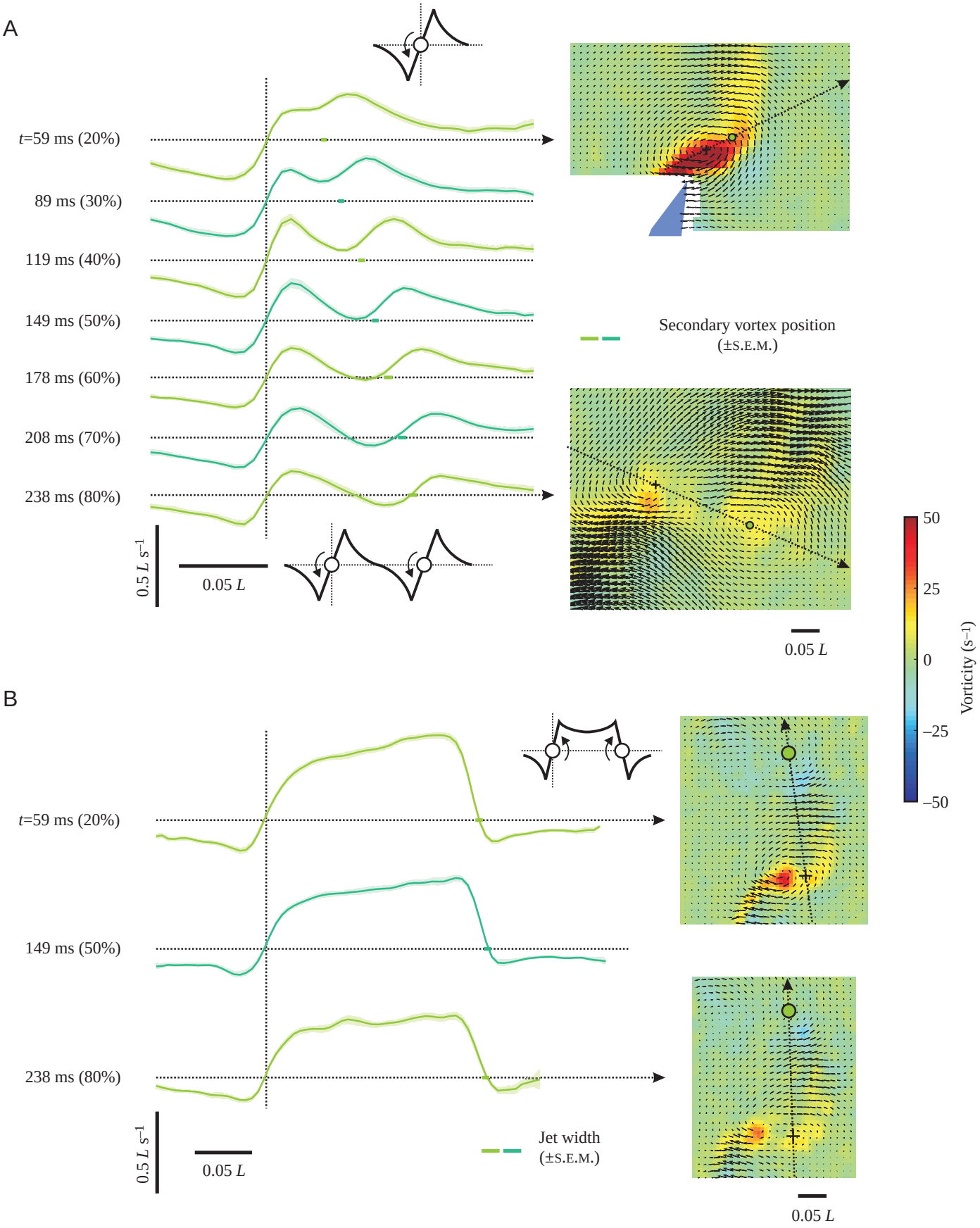
A
t=59 ms (20%)
89 ms (30%)
119 ms (40%)
149 ms (50%)
178 ms (60%)
208 ms (70%)
238 ms (80%)
0.5 L s⁻¹
0.05 L
Secondary vortex position
(±S.E.M.)
0.05 L
50
25
0
–25
–50
Vorticity (s⁻¹)
B
t=59 ms (20%)
149 ms (50%)
238 ms (80%)
0.5 L s⁻¹
0.05 L
Jet width
(±S.E.M.)
0.05 L

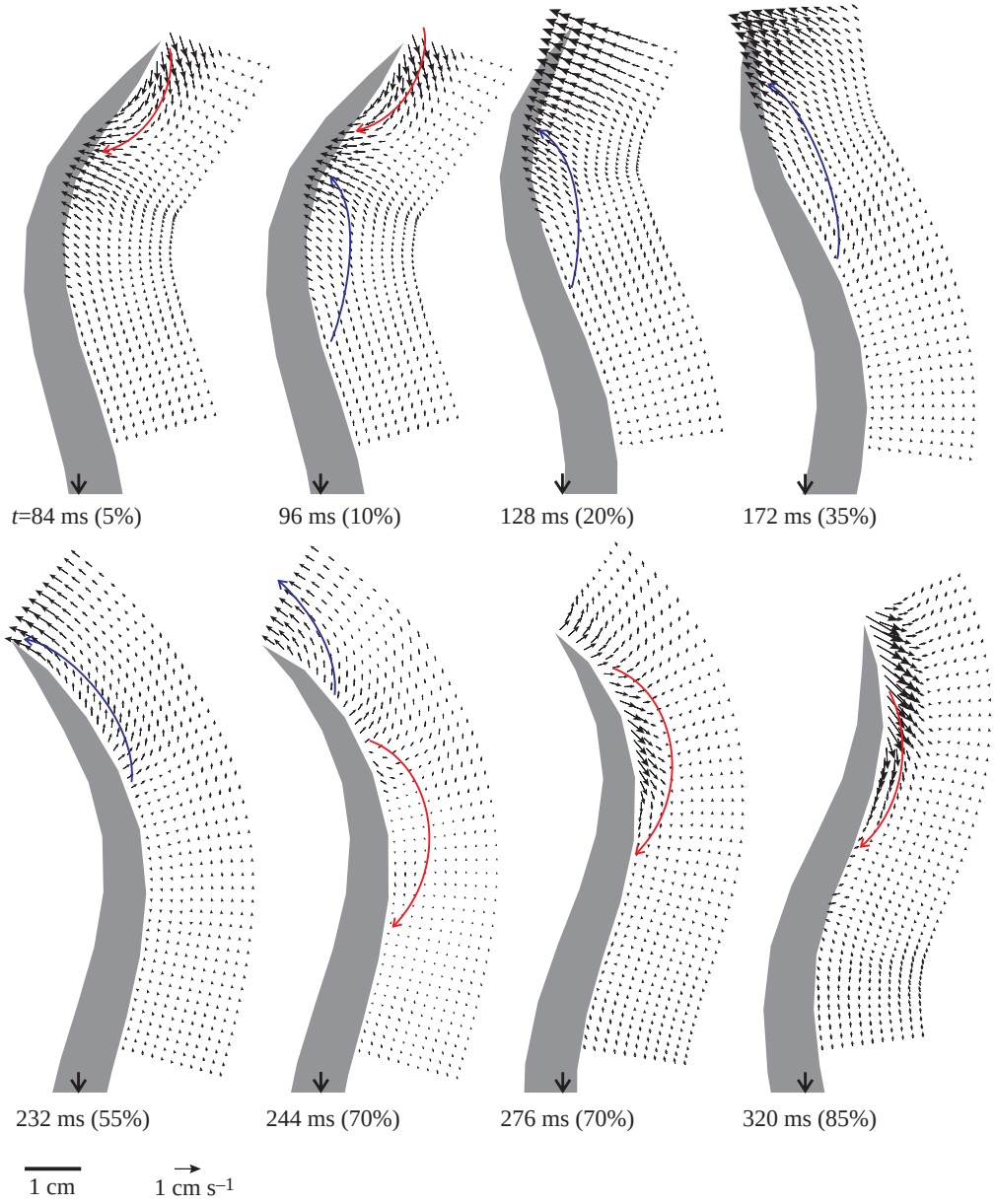

Fig. 7. Flow fields close to the body of a swimming eel, shown in gray. The lateral position of the eel's snout (off the view) is shown as a black arrow. Velocities are phase averaged across 14 tail beats by interpolating the normal gridded coordinate system on to a system defined by the distance from the eel's body and the distance along the body from the head. Approximate positions of the proto-vortices, defined by Müller et al. (2001), are shown in red (clockwise rotation) and blue (counter-clockwise rotation).

different from 90°; $P<0.001$). There is a trend for the jet to rotate downstream over time, but it is not significant ($F_{1,2}=1.860$; $P=0.306$). The peak velocities in the jet decrease significantly over time ($F_{1,2}=24.0$; $P=0.039$), diminishing by ~15% over a half tail beat, from 0.45 to 0.38 L s^{-1}. By contrast, the circulation measured through the center of the lateral jet does not change over time ($F_{1,2}=1.536$; $P=0.349$), remaining at 2490±10 cm^2 s^{-1}.

To illustrate the rolling up of the unstable shear layer, we took cross-sections through the primary and secondary vortices over time (Fig. 6A). The idealized profile through a single Rankine vortex (Faber, 1995) is shown above the first profile and a profile through two same-sign vortices is shown below the last profile. Additionally, Fig. 6B shows cross-sections across the lateral jet over time, with an ideal profile through a small-core vortex ring.

The circulations of the primary and secondary vortices both decrease over time. In principle, total circulation should remain constant, implying that the sum of the two circulations should not change over time. A repeated-measures ANOVA (Zar, 1999) in which the repeated measure was tail-beat phase divided into early and late regions shows that the initial circulation of the primary vortex alone, 3300 cm^2 s^{-1}, is not significantly different from the sum of the primary and secondary circulations in the end, 1910 cm^2 s^{-1} and 1520 cm^2 s^{-1}, respectively ($F_{1,89}=1.471$; $P=0.228$).

To examine how the wake is generated, flow close to the bodies of the eels was examined. Fig. 7 shows a typical flow pattern near the body of an eel over the course of a tail beat. In the first three frames shown, a strong suction region develops near the tail, pulling a bolus of fluid laterally. This bolus will become the lateral jet in the wake. Proto-vortices are

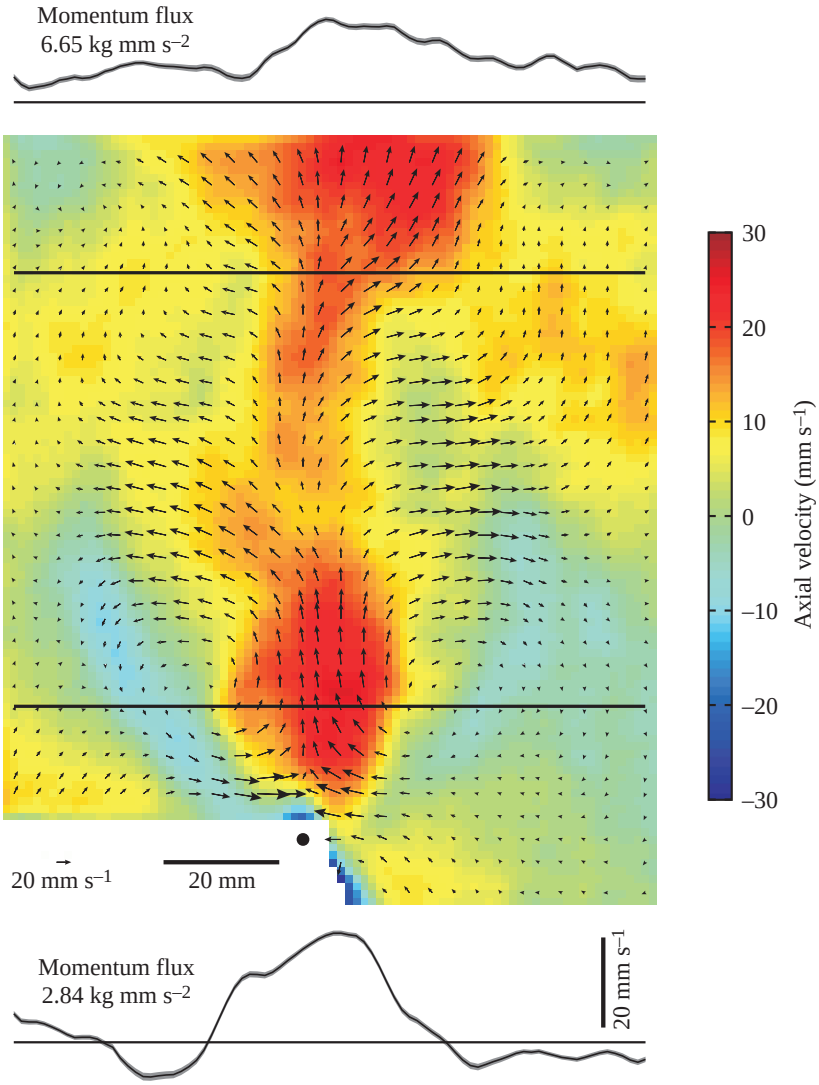

Fig. 8. Flow field behind the eel, averaged over 14 complete tail beats, centered on the tip of the eel's tail, shown as a black circle. Arrow heads are retained for velocities lower than 6.5 mm s^{-1} to indicate flow direction. Axial flow is shown in color: red is downstream and blue is upstream. Two profiles of velocity are shown in black above and below the flow field, with standard error in gray and total momentum flux represented by the trace printed beside it. Black lines across the field indicate where the velocity traces were measured (25 mm and 95 mm behind the tail). The vertical scale is the same for both traces.

visible (shown with red and blue arrows), but their vorticity is very low (generally less than ±5 s^{-1}).

Finally, for comparison with the computational model of Carling et al. (1998), we computed an average flow behind the eel, averaged over many tail beats. The computational model predicts a net velocity deficit behind the eel that could be obscured by the temporal variations in the observed flow. Fig. 8 shows the flow behind an eel averaged over 14 tail beats with axial flow magnitude shown in color. On average, momentum in the wake was elevated above free-stream momentum by between 2.84 and 6.65 kg mm s^{-2} at planes 25 mm and 95 mm, respectively, behind the tail.

Force, impulse and power

Impulses were calculated from PIV using equation 6 by assuming that the observed vortex cores were part of a small-core vortex ring. In equation 6, rather than using the circulation of one of the cores, which vary over time and are sensitive to digitization error, we chose to use the circulation measured through the center of the lateral jet, which is constant over time and fairly robust to digitization error. Thus, the impulse coefficient for the lateral jets was 0.0217±0.0004, corresponding to an impulse in a 20 cm eel of 0.76 mN s. From this value, given that the lateral jet was generated over half a period, the lateral force coefficient was 0.097±0.001 (4.64 mN in a 20 cm eel). Fig. 9A shows a typical trace of lateral force from EBT with the average force estimates from PIV superimposed; Table 2 displays the same comparison numerically.

Power was also measured in the wake at a plane approximately 8 mm downstream of the tail tip. Both total power, including both velocity components, and 'lateral' power, including only the lateral (v) velocity component, were calculated. Fig. 9B shows a typical trace of power over time. The total power coefficient was, on average, 0.023±0.002 (303 μW in a 20 cm eel). Lateral power was usually less than half of the total power and was equal to 0.0151±0.0003 (198 μW). Table 2 summarizes the comparison of force, impulse and power measurements from PIV with those calculated *via* EBT.

In general, EBT underestimates force and power as measured by PIV, although for certain values the two match well (Fig. 9). Both the impulse and the total wake power estimated by PIV and EBT are highly significantly different (P<0.001 in both cases; Table 2). However, the mean force from the PIV measurements matches the peak lateral force estimated by EBT (P=0.182). Additionally, the power estimated using only the lateral component of velocity is not significantly different from the total EBT estimate, in both maximum (P≈1.000) and mean values (P=0.693). The shape of these two power curves is also visually quite similar (Fig. 9B).

Discussion

This study provides a detailed picture of a typical anguilliform swimmer's wake during steady swimming at moderate swimming speeds. The wake consists of strong lateral jets, separated by two same-sign vortices (Fig. 10): probably unlinked vortex rings heading in opposite lateral

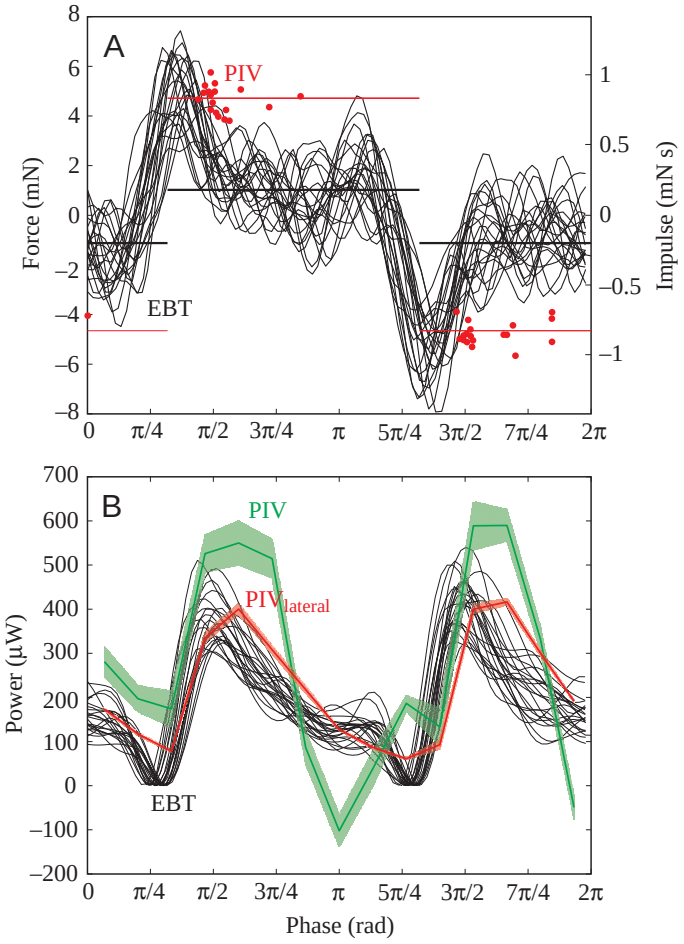

Fig. 9. Representative traces for force, impulse and power from large-amplitude elongated body theory (EBT; in black) and particle image velocimetry (PIV; in red and green). Each black line shows force and power for a single tail beat. A total of 14 tail beats from a single swimming bout are shown. (A) Force (left axis) and impulse (right axis) over a tail-beat cycle. Because impulse is force integrated over time, impulses are indicated as lines, showing the impulse value and the time over which it was integrated. (B) Power from EBT and PIV over a tail-beat cycle. PIV values have standard error in a lighter color around the trace. The total power measured through PIV is shown in green, and the 'lateral' power, measured using only the lateral velocity component, is shown in red.

directions. The most striking feature of the wake is the size and strength of the lateral jets and the notable absence of substantial downstream flow. In contrast to the downstream flow observed in the wakes of carangiform swimmers, almost all of the flow in an eel's wake is in jets directed laterally.

The lateral jets are produced along the body, just anterior to the tail tip. In particular, when the tail has reached its maximum lateral excursion, and thus has zero velocity, the point 0.15 L anterior to the tail has reached a high lateral velocity (60.2±0.6% of the swimming velocity). This substantial velocity difference along the eel's body seems to result in a strong suction region that pulls fluid laterally. Once the tail changes direction, it sheds a stop/start vortex (the primary vortex) and begins to shed a bolus of fluid to form a lateral jet. Each full tail beat produces two jets, one to each side, and two vortices separating them.

Because the velocities in successive lateral jets are large and in opposite directions, a substantial shear layer is present between the jets, with shearing rates of as much as 90 s^{-1}. This shear layer is unstable and breaks down into two or more vortices (the secondary vortices), probably through a Kelvin–Helmholtz instability (Faber, 1995). This instability develops gradually (Fig. 6A), resulting in a fully formed secondary vortex about one full cycle later. Classic hydrodynamic theory predicts that a Kelvin–Helmholtz instability should result in vortices with a spacing approximately equal to $4\pi\delta$, where δ is the shear layer thickness (Faber, 1995). Before the shear layer breaks down, δ is approximately 3 mm, giving a predicted vortex spacing of 37 mm, which is close to the 20–30 mm spacing observed when the secondary vortex is fully formed. Additionally, the theory suggests that many vortices with this spacing could be formed. Indeed, another secondary vortex is occasionally formed at about twice the distance from the primary vortex.

Table 2. *Comparison of force, impulse and power from PIV and EBT*

	PIV coefficient	Dimensional	EBT coefficient	Dimensional	$F_{1,2}$	P
Lateral force*	0.097±0.001	4.64 mN	0.090±0.003	4.31 mN	0.490	0.556
Lateral impulse	**0.0217±0.0004**	**0.76 mN s**	**0.0062±0.0001**	**0.216 mN s**	**36.18**	**0.027**
Thrust force†			0.0166±0.0004	0.79 mN		
Max. lateral power	0.0297±0.0007	391 μW	0.0286±0.0005	376 μW	0.103	0.778
Mean lateral power	0.0151±0.0003	198 μW	0.0148±0.0003	195 μW	0.200	0.699
Max. total power	**0.065±0.003**	**855 μW**	**0.0286±0.0005**	**376 μW**	**16.25**	**0.056**
Mean total power	0.023±0.002	303 μW	0.0148±0.0003	195 μW	0.292	0.643

Bold indicates a significant difference.

P values are calculated including individuals as a random effect. The individual was a significant effect in all comparisons (P<0.001) except for lateral force (P=0.090). N=118.

Dimensional values are calculated from the coefficients for a 20 cm-long eel.

*Compares mean lateral force from particle image velocimetry (PIV) to peak value from elongated body theory (EBT).

†Thrust force could only be calculated using EBT.

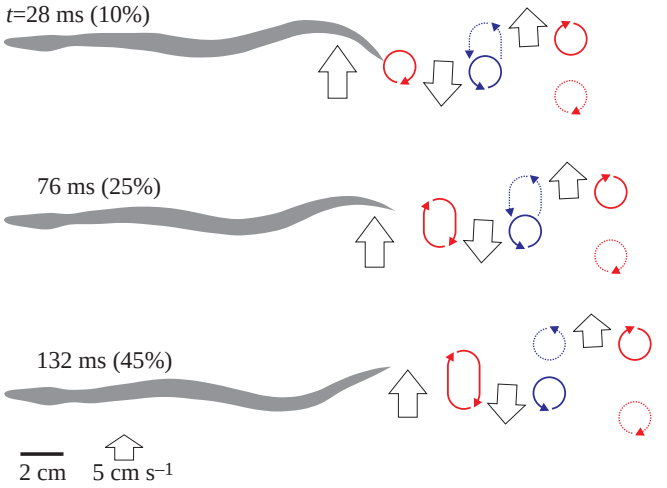

Fig. 10. Schematic summary of the results of the present study, showing the wake behind a swimming eel at three different times. The size of the eel and position of the vortices are scaled to represent the true spacing. Vortices are indicated by blue and red arrows; primary vortices are solid lines and secondary vortices are dotted lines. The lateral jets are shown as block arrows, with lengths and angle proportional to the jet magnitude and direction.

When the jets are fully developed, they point almost directly laterally, meaning that very little flow is directed axially. Previous studies of caudal fin swimming (e.g. Müller et al., 1997; Lauder and Drucker, 2002; Nauen and Lauder, 2002a) have interpreted axial downstream flow as evidence for the production of thrust and have found that estimates of the thrust from PIV approximately match the estimated drag on the fish (Lauder and Drucker, 2002). This balance also held true for fish swimming using their pectoral fins (Drucker and Lauder, 1999). If downstream velocity is evidence for thrust, where is the thrust signature in the eel wake?

Because the eels in the present study were swimming steadily, without any substantial accelerations, the net force on the animal must be zero and, thus, the net force measurable in the wake should also be zero. Equivalently, because the momentum of the eel is not changing, there must be no net change in fluid momentum. Thus, while somewhat counter-intuitive, it is physically reasonable that no downstream momentum jet would be evident in the wake. It is important to think of the eel as producing thrust and drag simultaneously. If one could separate thrust from drag, one would see fluid being accelerated down the eel's body, as it produces thrust. At the same time, however, the drag along the eel's body is removing momentum from the fluid. In combination, the two effects cancel each other out, producing no net change in downstream fluid momentum as long as the eel is swimming steadily. All the lateral momentum observed in the wake also cancels out and is simply evidence of wasted energy.

If thrust and drag balance exactly, why did we observe a small increase in downstream momentum immediately behind the tail (Fig. 8)? Probably, this increase is offset by an increase in the opposite direction at the eel's snout. In still water, an eel swimming forward would push some fluid out of its way with its snout, increasing the upstream fluid momentum (Long et al., 2002). For forces to balance, this upstream increase must be matched by a small downstream increase at the tail, as we observed. The eel's snout adds upstream momentum at a rate proportional to $\rho U a_{\mathrm{head}}$, where a_{head} is an area at the snout, representing a force in the order of 5 mN. The extra downstream momentum in the wake represents forces between 3.5 and 7.5 mN, which are roughly in agreement. We thus argue that the additional downstream momentum observed in the eel wake (Fig. 8) is necessary to fully conserve momentum and is not evidence for thrust. A complete control volume around the eel would resolve this question fully, but eels would not swim steadily with their heads in the light sheet, preventing us from performing that additional experiment.

It is important to note that the lack of net change in momentum is not equivalent to 'leaving no footprints', as hypothesized by Ahlborn et al. (1991). The 'footprints' of an eel are the lateral jets. In principle, at 100% efficiency, as Ahlborn et al. (1991) suggested, all power would go into producing forward motion, and none would go into producing a wake. The fact that an eel does leave a wake, or footprints, is evidence that they are not completely efficient.

This momentum balance described above must be true for all steady swimming, including previous studies that have observed a strong downstream jet during carangiform and pectoral fin swimming (Müller et al., 1997; Drucker and Lauder, 2000; Lauder and Drucker, 2002; Nauen and Lauder, 2002a). It is our hypothesis that these previously studied fishes display some spatial or temporal separation between thrust and drag production that allows momentum to balance on average over a tail beat, while still producing a downstream jet indicating thrust. The apparent discrepancy between this study and these previous ones is easiest to explain for pectoral fin swimmers. Drucker and Lauder (2000) observed a downstream jet from pectoral fin swimming in bluegill sunfish (*Lepomis macrochirus*) and surf perch (*Embiotoca jacksoni*) that represented enough force to balance the experimentally measured drag. Unlike eels, bluegill and surf perch rely solely on their pectoral fins for thrust in the speed range examined. Pectoral fins effectively produce only thrust and little drag, relative to the body, which is held nearly motionless at these swimming speeds and produces only drag. The spatial separation between the thrust-producing pectoral fins and the drag-producing body allows accurate measurement of thrust from the pectoral fins alone, as Drucker and Lauder (2000) found. Nonetheless, if one were to examine a control volume around the entire fish, the net fluid momentum change would be zero. The situation is somewhat like that of an outboard propeller on a boat: the body, like a boat's hull, generates most of the drag and negligible thrust, and the pectoral fins, like propellers, generate all of the thrust with negligible drag.

For carangiform caudal fin swimmers, the situation is more complicated, but previous results should still be valid. For many fishes, the outboard motor analogy may still be appropriate. Because carangiform swimmers move their

anterior body relatively little compared to the caudal fin (Webb, 1975; Jayne and Lauder, 1995; Donley and Dickson, 2000), very little thrust can be generated anterior to the caudal peduncle. Flow also does not separate along the body (Anderson et al., 2000) but rather converges on the caudal peduncle (Nauen and Lauder, 2000). As fluid moves along the body, drag removes momentum, but this low-momentum flow is concentrated at the caudal peduncle. The dorsal and ventral portions of the caudal fin are therefore exposed primarily to undisturbed free-stream flow. Except at the very center of the fin, the caudal fin thus may also function like an outboard motor, producing almost entirely thrust with very little drag. Probably the analogy is most valid for fishes such as mackerels and tunas that have a very narrow caudal peduncle and a large caudal fin. Indeed, in their study of chub mackerel (*Scomber japonicus*), Nauen and Lauder (2002a) found that thrust measured from the downstream jet roughly balanced experimentally measured drag (although drag measurements were difficult to make accurately).

For carangiform swimmers with less pronounced caudal peduncles, the outboard motor analogy may break down somewhat, but differences in swimming kinematics between them and anguilliform swimmers may explain why thrust wakes were still observed (e.g. in Müller et al., 1997; Drucker and Lauder, 2001). We speculate that anguilliform swimmers may produce thrust more continuously over time than carangiform swimmers. For a steadily swimming fish, thrust need only balance drag on average over a full tail beat. If thrust is produced in a very pulsatile way, it may briefly exceed drag to such an extent that it would be evident in the wake. According to a reactive inviscid theory such as Lighthill's EBT (Lighthill, 1971), thrust is only produced at the tail tip (or other sharp trailing edges). Evaluation of the EBT equation for thrust generated at the tail tip (equation 1) results in a pulsatile force. However, these equations do not include possible thrust from the body anterior to the tail due to viscous effects. Recent direct numerical simulations showed that an infinitely long waving plate can produce thrust (Shen et al., 2003), in support of previous experimental observations (Taneda and Tomonari, 1974; Techet, 2001). Like a waving plate, the short wavelength undulations along an eel's body can produce thrust smoothly to even out the pulsatile force from the tail tip. In particular, since a full wavelength is present on the eel's body, a portion of the body is moving and likely producing force out of phase with the tail tip. The majority of thrust may still be produced in the posterior regions of the eel's body, where we saw accelerated flow (Fig. 7) but, even so, some regions of the posterior body are moving out of phase with the tail tip, helping to smooth out pulsatile thrust. For carangiform swimmers, unlike eels, the long wavelength body undulations do not contain out-of-phase motions at sufficient amplitude and may tend to reinforce the pulsatile thrust from the tail (Webb, 1975). Therefore, at certain points in a carangiform swimmer's tail beat, thrust may exceed drag to produce a thrust wake, even though the two forces balance on average. For eels, thrust and drag may balance more evenly over time. Note that Fig. 9 does not contradict this statement. Fig. 9 shows that lateral force and power are pulsatile, but axial force was not measurable and 'axial power', constructed in a similar way to 'lateral power', remains fairly constant and small over the tail beat.

The importance of shape

We speculate that the novel wake structure of swimming eels is highly dependent on their shape and that differences in shape, along with differences in kinematics, may be one of the primary distinctions between anguilliform and carangiform swimming. In particular, eels do not have a narrow caudal peduncle, whereas most carangiform swimmers do. The large lateral jets develop in the suction region centered around ~85% of body length. Both anguilliform and carangiform swimmers have a substantial undulation amplitude this close to the tail, even though the kinematics on the anterior body differ substantially. For example, both chub mackerel and kawakawa tuna (*Euthynnus affinis*) have amplitudes of ~4% of body length at 0.85 *L* (Donley and Dickson, 2000), and largemouth bass (*Micropterus salmoides*) have amplitudes of ~4.5% at 0.85 *L* (Jayne and Lauder, 1995), comparable with the 4.4% we measured in eels. However, most carangiform swimmers are different from eels because they have a narrow caudal peduncle around 0.85 *L*. If their body shape were more similar to that of eels, it is likely that a substantial suction could develop there in the same way as in eels. The narrowness of the peduncle, however, probably prevents such suction from developing. Even if a mackerel, for example, swam using the same kinematics as an eel, its wake would probably differ from an eel's due to the differences in body shape. In fact, recent results from an engineering study of rectangular flapping membranes indicate that simple shape differences, such as the ratio of flapping amplitude to body height, can determine whether the wake is a linked vortex ring wake, as observed in carangiform swimmers, or an unlinked ring wake, as in eels (J. Buchholz, personal communication).

Clearly, this effect in fishes is more complicated than a simple ratio and probably depends on how narrow the peduncle is, relative to the size of the body and tail. It would therefore be strongly affected by the wide range of body shapes in fishes. Wakes, therefore, probably show a gradation from those of mackerel (Nauen and Lauder, 2002a), for example, which have very narrow peduncles but large caudal fins, to those of eels, which have no narrowing at the peduncle at all.

Efficiency of anguilliform swimming

One of the goals of the present study was to evaluate the efficiency of anguilliform swimming relative to carangiform swimming. However, for steady swimming, efficiency is very hard to evaluate. Froude efficiency (η) is usually written, neglecting inertial forces, as:

$$\eta = \frac{\text{Useful power}}{\text{Total power}} = \frac{FU}{FU + P_{\text{wake}}}, \quad (9)$$

where F is a force, U is the swimming velocity and P_{wake} is the power in the wake (Webb, 1975). Strictly, F is the net force

on the swimming body, which is zero during steady swimming, resulting in a zero Froude efficiency. Schultz and Webb (2002) have discussed this issue in some detail. If F is the thrust force only, then η represents how much power was used for thrust and how much was wasted. While thrust cannot be measured directly from the wake of swimming eels, it is still useful, conceptually, to separate it from drag. By using a mathematical model, such as EBT or more complex computational fluid dynamic models (Carling et al., 1998; Wolfgang et al., 1999; Zhu et al., 2002), thrust can be estimated and used to calculate a Froude propulsive efficiency.

Specifically, EBT can be used to calculate this thrust value using equation 1, which can be combined with the wake power estimate from PIV to produce an efficiency. The estimated mean thrust is 0.83 mN, and the measured wake power is between 198 and 303 μW, resulting in efficiency estimates between 0.43 and 0.54. Additionally, EBT can also estimate the efficiency directly. This value, η_{EBT}, is usually written as $1-\frac{1}{2}(V-U)/V$, where V is the body wave velocity (Lighthill, 1970). According to this method, EBT estimates η_{EBT} as 0.865±0.001. However, since EBT usually underestimated the total power in the wake (Table 2), the first range, 0.43–0.54, is probably the more realistic estimate.

Anguilliform swimming has been hypothesized to be inefficient (Lighthill, 1970; Webb, 1975). Our measurements, however, indicate a swimming efficiency of around 0.5, or potentially as high as 0.87, depending on how it is calculated. Because of the difficulties of estimating efficiency from a steadily swimming fish, it is difficult to compare this value with previously reported values, which range from 0.74 to 0.97 (Drucker and Lauder, 2001; Müller et al., 2001; Nauen and Lauder, 2002a,b).

Comparison with previous studies of anguilliform swimming

Müller et al. (2001) first observed the wakes of swimming eels and noted their unusual structure. They showed that two vortices were produced per half tail beat and that the jet between successive vortices was primarily lateral. Their observations are, in general, quite similar to ours. With our higher resolution PIV, we are able to propose a different mechanism for generating the wake. Additionally, our data allowed a much more detailed examination of the balance of thrust and drag and the Froude efficiency of steady swimming, which have been controversial (Schultz and Webb, 2002).

Nonetheless, there are some important differences between our findings and those of Müller et al. (2001). They hypothesized that the double vortex structure resulted from a phase lag between the vorticity shed from the tail and circulation produced along the body, which they termed proto-vortices. Although proto-vortices were evident along the body (Fig. 7), their vorticity was much lower than the vorticity of the secondary vortex. The vorticity in the proto-vortices along the body is generally less than 5 s^{-1}, while the secondary vortex peak vorticity was often more that 15 s^{-1}. Müller et al. (2001) also observed that fluid velocity increases along the body linearly from head to tail. By contrast, we observed relatively little increase in fluid velocity until the last 30% of body length, where the fluid bolus is generated (Fig. 7). Finally, we calculated the phase difference between the shedding of stop/start vortices and the shedding of proto-vortices off the tail. The difference was only ~5% of a tail beat cycle, so any proto-vorticity is likely to simply add to the stop/start vortex, which is forming at almost the same time, rather than create a separate vortex.

It is somewhat surprising that we saw so much less fluid velocity along the body than Müller et al. (2001) did. While the eels analyzed in detail in the present study, at 20 cm long, were more than twice as long as those in Muller's study, we examined the wake of a 12 cm eel qualitatively and found the same pattern as in the larger eels. The eels in Müller's study seemed to show greater undulation amplitude along the body, particularly near the head, than the eels in our study. This amplitude difference may explain the stronger fluid flow near the body but it also suggests that Müller's eels may have been accelerating slightly, because increased anterior undulation is often found in accelerating eels (E. D. Tytell, manuscript in preparation). Additionally, they document a slight downstream component to the jets (Müller et al., 2001), another indication of acceleration (E. D. Tytell, manuscript in preparation).

The other model examined in the present study, Carling and colleagues' computational fluid dynamic model for an 8 cm-long anguilliform swimmer (Carling et al., 1998), is not supported by our data or those of Müller et al. (2001). Carling's model predicts a substantially reduced velocity immediately behind the tail, as if the eel were sucking fluid along with it as it swam (Fig. 1B). Even averaged over many tail beats, we did not observe any reduced velocity in the wake; in fact, immediately behind the tail, the flow is accelerated downstream (Fig. 8). Somewhat surprisingly, we observed that momentum in the far wake, 95 mm from the eel's tail, was greater than that in the near wake, 25 mm from the tail. We speculate that this effect is due to three-dimensional reorientation or contraction of the wake, similar to that in the far-field wake of a hovering insect (Ellington, 1984). Nonetheless, it seems clear that axial wake momentum is downstream, the opposite of what the model predicted (Carling et al., 1998). Additionally, their model does not predict the complex vortical structures and lateral jets that we consistently observed in all individuals covering a length range from 12 to 23 cm. While we did not observe the wake of an 8 cm individual, the size they modeled, Müller et al. (2001) examined one that size and observed a wake similar to those we observed in larger individuals and quite different from Carling and colleagues' predictions (Carling et al., 1998).

To continue the exploration of the hydrodynamic differences between different modes of swimming, future studies should be careful to include detailed kinematics. Small differences in kinematics may cause substantial changes in flow, as we noted in the differences between Müller et al. (2001) and our study. This effect may prove useful, however: small kinematic differences as fishes change swimming speed may induce large hydrodynamic changes, as seen in pectoral fin swimming

(Drucker and Lauder, 2000). Examining both effects simultaneously will help to elucidate the mechanical effect of changing kinematics with swimming speed and between different swimming modes.

We would like to thank Thelma Williams and John Carling for stimulating our interest in anguilliform hydrodynamics, Ulrike Müller for productive discussions of the interaction between kinematics and wake structure, and Paul Webb for many ideas and thoughts on the balance of thrust and drag. Promode Bandyopadhyay, L. Mahadevan and Peter Madden provided comments on a draft of the manuscript, and Tonia Hsieh, Jimmy Liao, Matt McHenry and Christoffer Johanssen were helpful for advice throughout this project. Alexander Smits and James Buchholz provided some thought-provoking information on the wake structure behind flapping membranes. We also owe thanks to Laura Farrell, who maintained the animals used in this study. This research was supported by the NSF under grants IBN9807021 and IBN0316675 to G.V.L.

References

Agüí, J. C. and Jiménez, J. (1987). On the performance of particle tracking. *J. Fluid Mech.* **185**, 447-468.

Ahlborn, B., Harper, D. G., Blake, R. W., Ahlborn, D. and Cam, M. (1991). Fish without footprints. *J. Theor. Biol.* **148**, 521-533.

Alexander, R. McN. (1983). The history of fish mechanics. In *Fish Biomechanics* (ed. P. W. Webb and D. Weihs), pp. 1-36. New York: Praeger.

Anderson, E. J., McGillis, W. R. and Grosenbaugh, M. A. (2000). The boundary layer of swimming fish. *J. Exp. Biol.* **204**, 81-102.

Barrett, D., Triantafyllou, M. S., Yue, D. K. P., Grosenbaugh, M. A. and Wolfgang, M. J. (1999). Drag reduction in fish-like locomotion. *J. Fluid Mech.* **392**, 183-212.

Breder, C. M. (1926). The locomotion of fishes. *Zoologica* **4**, 159-297.

Carling, J. (2002). Numerical approaches in computational fluid dynamics. *Comp. Biochem. Physiol. A* **132**, S85.

Carling, J., Williams, T. L. and Bowtell, G. (1998). Self-propelled anguilliform swimming: simultaneous solution of the two-dimensional Navier–Stokes equations and Newton's laws of motion. *J. Exp. Biol.* **201**, 3143-3166.

Donley, J. M. and Dickson, K. A. (2000). Swimming kinematics of juvenile kawakawa tuna (*Euthynnus affinis*) and chub mackerel (*Scomber japonicus*). *J. Exp. Biol.* **203**, 3103-3116.

Donley, J. M. and Shadwick, R. E. (2003). Steady swimming muscle dynamics in the leopard shark *Triakis semifasciata*. *J. Exp. Biol.* **206**, 1117-1126.

Drucker, E. G. and Lauder, G. V. (1999). Locomotor forces on a swimming fish: three-dimensional vortex wake dynamics quantified using digital particle image velocimetry. *J. Exp. Biol.* **202**, 2393-2412.

Drucker, E. G. and Lauder, G. V. (2000). A hydrodynamic analysis of fish swimming speed: wake structure and locomotor force in slow and fast labriform swimmers. *J. Exp. Biol.* **203**, 2379-2393.

Drucker, E. G. and Lauder, G. V. (2001). Locomotor function of the dorsal fin in teleost fishes: experimental analysis of wake forces in sunfish. *J. Exp. Biol.* **204**, 2943-2958.

Ellington, C. P. (1984). The aerodynamics of hovering insect flight. V. A vortex theory. *Phil. Trans. R. Soc. Lond. B* **305**, 115-144.

Faber, T. E. (1995). *Fluid Dynamics for Physicists*. Cambridge: Cambridge University Press.

Fincham, A. M. and Spedding, G. R. (1997). Low cost, high resolution DPIV for measurement of turbulent fluid flow. *Exp. Fluids* **23**, 449-462.

Gillis, G. B. (1998). Environmental effects on undulatory locomotion in the American eel *Anguilla rostrata*: kinematics in water and on land. *J. Exp. Biol.* **201**, 949-961.

Hart, D. P. (1999). Super-resolution PIV by recursive local-correlation. *J. Visual.* **10**, 1-10.

Hart, D. P. (2000). PIV error correction. *Exp. Fluids* **29**, 13-22.

Helfman, G. S., Collette, B. B. and Facey, D. E. (1997). *The Diversity of Fishes.* London: Blackwell Science.

Jayne, B. C. and Lauder, G. V. (1995). Speed effects on midline kinematics during steady undulatory swimming of largemouth bass, *Micropterus salmoides*. *J. Exp. Biol.* **198**, 585-602.

Lauder, G. V. (2000). Function of the caudal fin during locomotion in fishes: kinematics, flow visualization, and evolutionary patterns. *Am. Zool.* **40**, 101-122.

Lauder, G. V. and Drucker, E. G. (2002). Forces, fishes, and fluids: hydrodynamic mechanisms of aquatic locomotion. *News Physiol. Sci.* **17**, 235-240.

Liao, J. (2002). Swimming in needlefish (Belonidae): anguilliform locomotion with fins. *J. Exp. Biol.* **205**, 2875-2884.

Lighthill, M. J. (1960). Note on the swimming of slender fish. *J. Fluid Mech.* **9**, 305-317.

Lighthill, M. J. (1970). Aquatic animal propulsion of high hydromechanical efficiency. *J. Fluid Mech.* **44**, 265-301.

Lighthill, M. J. (1971). Large-amplitude elongated-body theory of fish locomotion. *Proc. R. Soc. Lond. A* **179**, 125-138.

Long, J. H., Root, R. G. and Watts, P. (2002). Is an undulating fish an oscillating wing? *Integ. Comp. Biol.* **42**, 1268.

Müller, U. K., van den Heuvel, B.-L. E., Stamhuis, E. J. and Videler, J. J. (1997). Fish foot prints: morphology and energetics of the wake behind a continuously swimming mullet (*Chelon labrosus risso*). *J. Exp. Biol.* **200**, 2893-2906.

Müller, U. K., Smit, J., Stamhuis, E. J. and Videler, J. J. (2001). How the body contributes to the wake in undulatory fish swimming: flow fields of a swimming eel (*Anguilla anguilla*). *J. Exp. Biol.* **204**, 2751-2762.

Nauen, J. C. and Lauder, G. V. (2000). Locomotion in scombrid fishes: morphology and kinematics of the finlets of the chub mackerel *Scomber japonicus*. *J. Exp. Biol.* **203**, 2247-2259.

Nauen, J. C. and Lauder, G. V. (2002a). Hydrodynamics of caudal fin locomotion by chub mackerel, *Scomber japonicus* (Scombridae). *J. Exp. Biol.* **205**, 1709-1724.

Nauen, J. C. and Lauder, G. V. (2002b). Quantification of the wake of rainbow trout (*Oncorhynchus mykiss*) using three-dimensional stereoscopic digital particle image velocimetry. *J. Exp. Biol.* **205**, 3271-3279.

Robinson, S. K. (1991). Coherent motions in the turbulent boundary layer. *Annu. Rev. Fluid Mech.* **23**, 601-639.

Schlichting, H. (1979). *Boundary-Layer Theory*. New York: McGraw-Hill.

Schultz, W. W. and Webb, P. W. (2002). Power requirements of swimming: do new methods resolve old questions? *Integ. Comp. Biol.* **42**, 1018-1025.

Shaffer, H. B. and Lauder, G. V. (1985). Patterns of variation in aquatic ambystomatid salamanders: kinematics of the feeding mechanism. *Evolution* **39**, 83-92.

Shen, L., Zhang, X., Yue, D. K. P. and Triantafyllou, M. S. (2003). Turbulent flow over a flexible wall undergoing a streamwise travelling wave motion. *J. Fluid Mech.* **484**, 197-221.

Smith, D. G. and Tighe, K. A. (2002). Freshwater eels. Family Anguillidae. In *Fishes of the Gulf of Maine* (ed. B. B. Collette and G. Klein-MacPhee), pp. 92-95. Washington: Smithsonian Institution Press.

Spedding, G. R. and Rignot, E. J. M. (1993). Performance analysis and application of grid interpolation techniques for fluid flows. *Exp. Fluids* **15**, 417-430.

Stamhuis, E. J. and Videler, J. J. (1995). Quantitative flow analysis around aquatic animals using laser sheet particle image velocimetry. *J. Exp. Biol.* **198**, 283-294.

Taneda, S. and Tomonari, Y. (1974). An experiment on the flow around a waving plate. *J. Phys. Soc. Japan* **36**, 1683-1689.

Techet, A. H. (2001). Experimental visualization of the near-boundary hydrodynamics about fish-like swimming bodies. *Ph.D. Dissertation*. Department of Ocean Engineering, Massachusetts Institute of Techology/Woods Hole Oceanography Institute, Cambridge, MA, USA.

Triantafyllou, M. S., Triantafyllou, G. S. and Yue, D. K. P. (2000). Hydrodynamics of fishlike swimming. *Annu. Rev. Fluid Mech.* **32**, 33-53.

Tytell, E. D. and Lauder, G. V. (2002). The C-start escape response of *Polypterus senegalus*: bilateral muscle activity and variation during stage 1 and 2. *J. Exp. Biol.* **205**, 2591-2603.

van Ginneken, V. J. T. and van den Thillart, G. E. E. J. M. (2000). Eel fat stores are enough to reach the Sargasso. *Nature* **403**, 156-157.

Vollmers, H. (1993). Analysing, depicting, and interpreting flow fields. *DLR-Nachrichten*, **70**, 2-8.

Walker, J. A. (1998). Estimating velocities and accelerations of animal locomotion: a simulation experiment comparing numerical differentiation algorithms. *J. Exp. Biol.* **201**, 981-995.

Webb, P. W. (1975). Hydrodynamics and energetics of fish propulsion. *Bull. Fish. Res. Bd. Can.* **190**, 1-159.

Westerweel, J., Dabiri, D. and Gharib, M. (1997). The effect of a discrete window offset on the accuracy of cross-correlation analysis of digital PIV recordings. *Exp. Fluids* **23**, 20-28.

Willert, C. E. and Gharib, M. (1991). Digital particle image velocimetry. *Exp. Fluids* **10**, 181-193.

Wolfgang, M. J., Anderson, J. M., Grosenbaugh, M. A., Yue, D. K. P. and Triantafyllou, M. S. (1999). Near-body flow dynamics in swimming fish. *J. Exp. Biol.* **202**, 2303-2327.

Zar, J. H. (1999). *Biostatistical Analysis*. Upper Saddler River, NJ: Prentice Hall.

Zhu, Q., Wolfgang, M. J., Yue, D. K. P. and Triantafyllou, M. S. (2002). Three-dimensional flow structures and vorticity control in fish-like swimming. *J. Fluid Mech.* **468**, 1-28.